

Circuit QED devices for probing Majorana zero modes

Oscar Erlandsson. Master's thesis.



LUND UNIVERSITY
Faculty of Science

Project carried out during the 2017-2018 academic year at
Center for Quantum Devices, Niels Bohr Institute, University of Copenhagen.

Supervisor: Charles Marcus (University of Copenhagen).

Co-supervisor: Martin Leijnse (Lund University).

Abstract

Theoretical understanding indicates that Majorana zero modes in solid-state systems could be utilized for fault-tolerant quantum information processing. The ability to reliably detect these excitations, however, remains a challenge and many of their properties are still unknown.

In this Master's project, devices that implement a circuit quantum electrodynamics architecture and are predicted to host Majorana zero modes have been fabricated and characterized at temperatures below 50 mK. Single-junction as well as split-junction geometries have been investigated. In neither case have the expected Majorana signatures been detected. A primary difficulty is operating the devices in magnetic fields large enough to induce the presence of Majorana zero modes. Effects in which the signatures are expected to occur, charge dispersion for the single-junction case and flux dependence for the split-junction case, have been resolved at in-plane fields of approximately 150 mT and 300 mT, respectively.

Although non-affirmative of the existence of Majorana states in the devices, the results represent a step toward detection and eventually utilization of Majorana zero modes in superconducting circuits.

Acknowledgements

The work described in the present Master's thesis has been conducted as part of a research project at the Center for Quantum Devices (QDev) at University of Copenhagen. The team working on this project has consisted of Thorvald Larsen, Anders Kringsøj, Lucas Casparis, Marina Hesselberg, Robert McNeil and myself, supervised by Karl Petersson and Charles Marcus. Sponsorship of facilities and staff within QDev was provided by the Danish National Research Foundation and Microsoft.

I am grateful for the help I have received from the persons mentioned above, as well as from all the great people at QDev in general.

List of abbreviations

AWG	arbitrary waveform generator
CPB	Cooper pair box
D/A	digital-to-analog converter
EBL	electron beam lithography
GPIB	general purpose interface bus
IC	integrated circuit
JJ	Josephson junction
LAN	local area network
MC	mixing chamber
MT	Majorana transmon
MZM	Majorana zero mode
PCB	printed circuit board
QED	quantum electrodynamics
SEM	scanning electron microscopy
SQUID	superconducting quantum interference device
TQC	topological quantum computation
VLS	vapor–liquid–solid
VNA	vector network analyzer

Contents

1	Introduction	1
2	Theory and background	4
2.1	Superconducting qubits and circuit QED	4
2.1.1	Cooper pair box and transmon	6
2.1.2	Circuit QED with transmission line resonator	8
2.1.3	Gate-tunable semiconductor nanowire transmon	11
2.2	Majorana zero modes in solid-state systems	11
2.3	Proposal for Majorana–transmon hybrid device	13
2.3.1	Aspects of physical realization	16
2.4	Qubit coherence and manipulation	17
3	Experimental method	19
3.1	Fabrication of qubit devices	19
3.2	Measurement setup with dilution refrigerator	20
3.3	Procedures for qubit characterization	22
4	Results	24
4.1	Single-junction qubit designed for $E_C/h = 230\text{MHz}$	24
4.2	Single-junction qubit designed for $E_C/h = 500\text{MHz}$	25
4.3	Split-junction qubit device	28
5	Discussion	31
5.1	Outlook	33
	Bibliography	34

Chapter 1 Introduction

A key aspect that has enabled the evolution of information technology is the miniaturization of devices making up the conventional classical computer. As the technology to fabricate transistors has improved, computation has been sped up due to more transistors working in parallel. Although these developments are sure to progress in the foreseeable future, the importance of quantum mechanical effects will be more significant the smaller these devices are made, which can interfere negatively with their performance. In addition, fundamental length scales, such as the size of individual atoms, seemingly constitute hard limits to miniaturization.

In parallel to these developments, the field of quantum computation, representing a fundamentally new way to perform computation, has developed rapidly in the more recent decades. The unit of information that quantum computers operate on is the quantum bit or *qubit*. Qubits are quantum mechanical two-level systems that can exist in any superposition of the ground state $|0\rangle$ and excited state $|1\rangle$. In general, the state $|\Psi\rangle$ of a qubit can be written on the form

$$|\Psi\rangle = \cos(\theta/2)|0\rangle + \exp(i\phi)\sin(\theta/2)|1\rangle \quad (1)$$

which allows for the visualization of the state as a point on the so called Bloch sphere in Fig. 1. The angle θ represents the balance of ground and excited state in the superposition and ϕ is a relative phase between them.

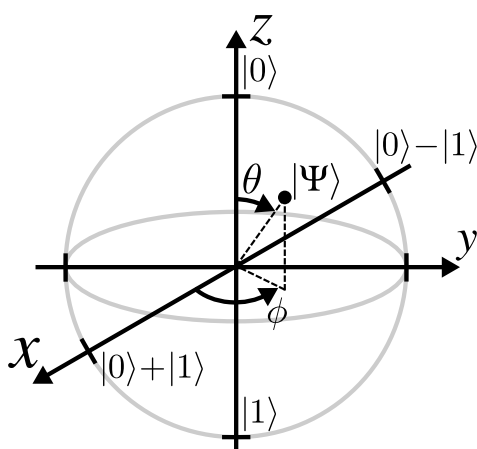


Figure 1: The Bloch sphere. The qubit state $|\Psi\rangle$ is represented by a point on the unit sphere.

Quantum computation directly exploits the superposition of states in order to parallelize computations. The field is now well-established [1] and it is theoretically known that once a

quantum computer has a sufficient number of qubits, it could outperform a classical computer at certain classes of problems, such as search algorithms, simulation and prime number factorization, the latter of relevance to cryptography.

Major research efforts have been invested in exploring candidate physical systems for the implementation of a qubit. The properties that these system must exhibit in order to facilitate full-scale quantum computation are famously summarized by the DiVincenzo criteria [2]. The fundamental criteria state that

1. the system must be scalable to very many qubits,
2. there should be a way to set these systems to their ground state,
3. the coherence times, which are measures of how long the qubit coherently remains in a given state, must be sufficiently long to perform the desired state manipulations,
4. there must exist known and executable operations associated with the system that can take it from any quantum state to another. This is known as a universal set of quantum gates.
Finally,
5. the state of the qubit should be measurable by a suitable method.

Notable categories of qubit implementations include trapped ions, spin states of nuclear magnetic resonances and qubits based on superconductivity. So far, no qubit implementation has been developed to the point of a quantum computer outperforming a classical computer.

In this thesis, a qubit system that builds upon a superconducting qubit is investigated. Superconducting qubits in general are extensively researched and exist in a variety of different kinds [3]. All types of superconducting qubits, however, feature the Josephson junction (JJ) element. This element provides *anharmonicity* to the energy levels, meaning that it makes them unevenly spaced. The reason that this is needed is that a qubit requires a transition between two states to be individually addressable, in order to move the system within a subset of only two states. The specific qubit system under investigation in this thesis builds upon the *transmon* qubit [4], implemented in a system for readout and control known as circuit quantum electrodynamics (circuit QED) [5]. The transmon qubit is a superconducting qubit utilizing a Josephson junction

and a large shunting capacitance. In circuit QED, interaction with the qubit is performed via standing waves in a superconducting resonator.

The need for long coherence times is one of the fundamental challenges associated with building a quantum computer. Typically, the state of the qubit is scrambled before a sufficient number of manipulations can be performed. The decoherence of qubits arise due to coupling to the environment, which can act as a decay channel for the excited state as well as introduce noise in the two-level system. These two interactions correspond to the relaxation time T_1 and dephasing time T_2^* , respectively.

In recent developments in condensed matter physics, a quasiparticle excitation known as a Majorana zero mode (MZM) has received much attention [6]. In part, this is due to the fundamental interest of the unique and fascinating properties of this excitation, such as being its own antiparticle. In addition to this interest, however, these properties are believed to have applications in quantum computation, offering a fundamental type of protection against decoherence. This field, called topological quantum computation (TQC), is still in its early development, with signatures compatible with MZMs having been detected in solid-state systems only recently [7].

The aim of the present project is to experimentally investigate a hybrid qubit system intended to combine the circuit QED transmon with the presence of MZMs. This hybrid is referred to as the Majorana transmon (MT) [8]. This system, while not protected against decoherence, could, if successfully implemented, reveal important properties about the nature of MZMs in superconducting circuits.

During the course of the project, several devices have been fabricated in a cleanroom environment, using conventional IC (integrated circuit) fabrication technology, such as electron beam lithography and metallization by sputtering. The finished devices have then been characterized by microwave experiments in a dilution refrigerator at temperatures below 50 mK.

The parts of the thesis following this introduction are divided into four chapters. In Chapter 2, the relevant theory of superconducting transmon qubits, Majorana zero modes and the Majorana transmon qubit is presented. In Chapter 3, the fabrication and measurement processes used in the project are described. Chapter 4 is dedicated to the obtained measurement results. Finally, the results and suggestions for future research are discussed in Chapter 5.

Chapter 2 Theory and background

In this chapter, the theory and background relevant for the project is presented. In the first section, an overview of superconducting circuits and qubits, as well as the circuit QED architecture, is given. In the following section, Majorana zero modes in condensed matter are introduced. In the third section, the specific theory for the hybrid devices of this project is presented. Finally, a section about the general aspects of qubit coherence and methods for probing it is included.

2.1 Superconducting qubits and circuit QED¹

Physical systems that are sufficiently isolated and cooled down are no longer approximated by classical physics; instead, good descriptions of their behavior are necessarily quantum mechanical. Superconductivity, the effect of zero electrical resistance in certain materials, allows for the flow of dissipationless currents. This means that superconducting circuits can remain at low temperature during operation, opening up the quantum regime to electrical circuits. Realizations of qubits based on quantum circuits can harness well-developed semiconductor technology, carrying its scalability and resolution of fabrication into quantum information processing applications.

The microscopic theory of superconductivity is known as BCS theory, due to its inventors J. Bardeen, L. N. Cooper and J. R. Schrieffer. The theory describes how an electron–electron interaction mediated by phonons opens up a superconducting gap Δ_S in the single electron spectrum and that electrons below this gap condensate into bosonic Cooper pairs. This condensate can support a zero resistance (dissipationless) supercurrent. The superconducting phase is preserved below a critical temperature T_c , current I_c and magnetic field B_c . Superconductivity constitutes a vast field of study within physics. In the following, aspects of superconductivity of particular relevance for the present are discussed.

In the 1960s, B. D. Josephson introduced theoretically what is now known as a Josephson junction (JJ). A JJ is three-part system in which a normal-state metal is positioned between two superconductors. Despite the weak link, such a junction can support a supercurrent, and the two

¹Parts of this section follow Ref. 9 fairly closely.

Josephson equations describing the system are

$$I = I_c \sin(\phi) \quad \text{and} \quad 2eV = \hbar \frac{\partial \phi}{\partial t} \quad (2, 3)$$

where ϕ , V and t are the quantum mechanical phase difference between the two superconductors, an applied voltage across the junction and time, respectively. The first equation describes the connection between the quantum properties of the Cooper pair condensates and a macroscopic supercurrent I . The second equation describes how the phase difference can be driven by applying a voltage bias.

In terms of how the supercurrent I depends on the magnetic flux Φ through the JJ, the junction can be thought of as a nonlinear inductor. For a regular inductor, the inductance $L = \Phi/I$ and in general $V = d\Phi/dt$. By analogy with these relations and Eqs. 2, 3, the Josephson inductance L_J is defined as

$$L_J = V \left(\frac{dI}{dt} \right)^{-1} = \frac{\hbar I_c}{2e \cos(2\pi\Phi/\Phi_0)} \quad (4)$$

where the constant $\Phi_0 = h/2e$ is called the flux quantum.

The nonlinear current–phase relation of the JJ is a unique addition to the standard circuit elements of resistors, capacitors and inductors. The general quantum mechanical description of superconducting circuits, can be motivated by considering the simple LC circuit. From electromagnetic theory, the energy E_{LC} stored in a regular LC circuit is $q^2/2C + \Phi^2/2L$ where q is the charge stored on the capacitor. Via the mapping $\Phi \rightarrow x$, $q \rightarrow p$, $C \rightarrow m$, where x , p and m are position, momentum and mass, respectively, the energy E_{LC} can be identified with the Hamiltonian of the quantum harmonic oscillator. By this identification, the fundamental quantum commutation relation for superconducting circuits can be inherited from the canonical position–momentum relation. The result is

$$[\hat{x}, \hat{p}] = [\hat{\Phi}, \hat{q}] = \hbar[\hat{\phi}, \hat{n}] = i\hbar \quad (5)$$

where the Cooper pair number operator $\hat{n} = \hat{q}/2e$ has been introduced. By these relations, equations describing electrical circuit can be quantized in terms of non-commuting operators.

A related aspect of superconductivity is the proximity effect, whereby a superconductor can induce superconductivity in a normal phase metal. By this effect, an energy gap opens up in the proximitized metal as well.

2.1.1 Cooper pair box and transmon

All superconducting qubits utilize the JJ described above. Conventionally, the superconducting qubits are classified into three categories depending on the degree of freedom used [3]. These categories are flux, phase and charge. The charge qubit is the relevant system for the project, and it will be introduced below.

The prototypical charge qubit is known as a Cooper pair box (CPB) and is illustrated schematically in Fig. 2a. In this system, one side of a Josephson junction forms an island hosting a quantized number \hat{n} of Cooper pairs each with charge $2e$. Cooper pairs can enter and leave the island by tunneling across the Josephson junction. The Hamiltonian describing the CPB is

$$\hat{H}_T = 4E_C(\hat{n} - n_g)^2 - E_J \cos(\hat{\phi}) \quad (6)$$

where $n_g = V_g C_g / 2e$ is the effective offset charge induced by the gate potential V_g through the capacitive coupling C_g and we have introduced the single-electron charging energy $E_C = e^2 / 2C$, where $C = C_g + C_J$ is the total capacitance of the island to ground, and the Josephson energy $E_J = I_C \Phi_0 / 2\pi$. An energy level diagram from a numerical diagonalization is displayed in the leftmost plot of Fig. 2c. The Hamiltonian can be understood simply as the stored energy in an LC circuit, where the (linear) inductance L has been replaced by the nonlinear Josephson inductance L_J , as defined in Eq. 4. If $E_J = 0$, the energy levels are parabolas as functions of n_g , reflecting the quadratic charge–energy relation of a capacitor for different quantized numbers \hat{n} of Cooper pairs on the island. A finite E_J opens anticrossings between charge parabolas representing integer numbers of Cooper pairs on the island.

The CPB qubit was first realized by the end of the 1990s [10, 11]. Although successfully demonstrated, the quantum mechanical coherence of this qubit was limited by charge-noise induced dephasing. Fluctuations of charge will inevitably occur in any solid-state device, making sensitivity to it a severe limitation. To some extent, dephasing of the CPB could be mitigated by operating qubits at extrema of the parabolic levels in Fig. 2c where first-order sensitivity to offset charge is vanishing. A more permanent solution was the introduction of the *transmon* (“transmission-line shunted plasma oscillation qubit”) by Ref. 4. The circuit diagram of this qubit device is displayed in Fig. 2b. The transmon is a modified version of the CPB featuring a

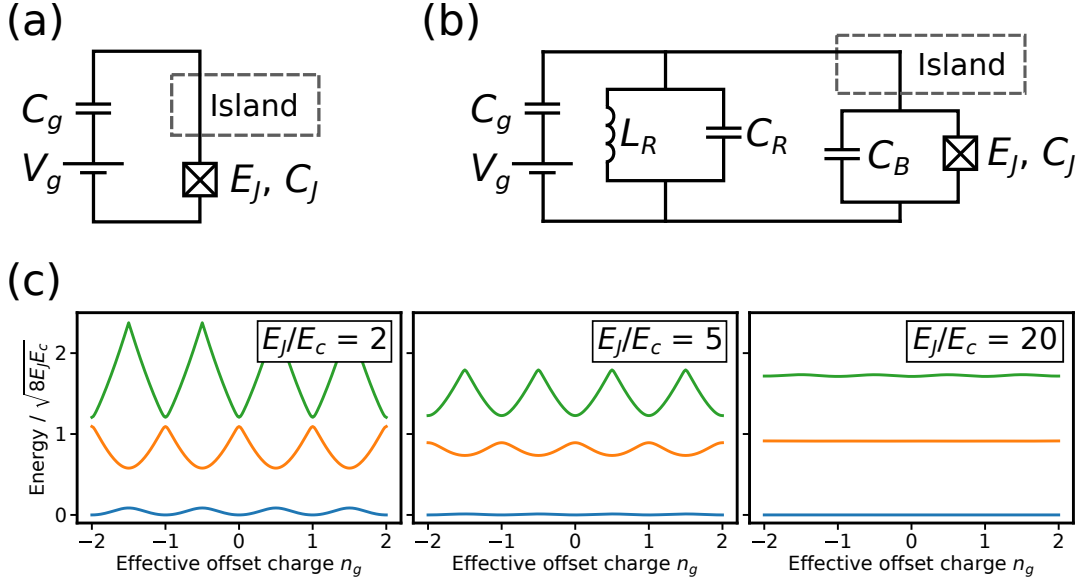


Figure 2: Circuit and energy level diagrams of superconducting charge qubits. Crossed boxes represent Josephson junction elements. (a) Cooper pair box. The charge of a superconducting island, coupled to ground via a Josephson junction, can be offset by a gate voltage V_g . (b) Transmon with shunting capacitance C_B . This transmon circuit also includes a superconducting resonator for circuit QED operation. (c) Energy level diagram of \hat{H}_T , describing both qubits. For a typical CPB, $E_J/E_C \approx 1$. Plots for increased E_J/E_C show the suppression of charge dispersion associated with the transmon. The energy minimum has been used as $E = 0$. Reproduction of plot in Ref. 4.

large shunting capacitance C_B across the Josephson junction, so that $C = C_g + C_J + C_B$. Due to the increased capacitance to the island, charging energy is decreased and the ratio E_J/E_C is increased. As apparent in Fig. 2c, this results in flattening the dependence of energy levels on n_g , which corresponds to an increase in the robustness against charge fluctuations. Increasing the ratio E_J/E_C to very high values also, however, decreases the anharmonicity (spacing between energy levels), which is shown and discussed in detail in Ref. 4. In that work, the (relative) anharmonicity α_r and charge dispersion ϵ_n are introduced, defined according to

$$\alpha_r = (E_{12} - E_{01})/E_{01} \quad \text{and} \quad \epsilon_n = \max E_n(n_g) - \min E_n(n_g) \quad (7, 8)$$

where $E_{mn} = E_n - E_m$ at $n_g = 1/2$ and E_i is the i th energy level (zero is ground state). Under the relevant circumstances, it is demonstrated that while increasing E_J/E_C leads to

an exponential suppression $\epsilon_n \propto \exp(-8E_J/E_C)$ but a power-law decrease in anharmonicity $\alpha_r \rightarrow -1/\sqrt{8E_J/E_C}$. These relations motivate qubit operation in the transmon regime $E_J/E_C \gg 1$. In discussing the devices of the present project, the absolute anharmonicity $\alpha = E_{12} - E_{01}$ is used, which in the transmon limit is shown to be given by

$$\alpha = -E_C . \quad (9)$$

The realization of a transmon qubit has been reported e.g. in Ref. 12. In that work, the introduction of single electrons in the superconducting system, often referred to as quasiparticle poisoning, can be observed in the experimental data. For a single electron to enter into the superconductor, an energy of the gap Δ_S must be supplied, which can happen in practice e.g. by thermal or radiative processes. Adding a single electron to the superconducting island of a transmon qubit shifts the island charge by $1e$. Therefore, in an experimental measurement which is slow compared to the poisoning timescale, the effect of poisoning is that each energy level in Fig. 2c will have a crossing curve offset by $\Delta\hat{n} = 1/2$ (half a Cooper pair).

2.1.2 Circuit QED with transmission line resonator

The DiVincenzo criteria discussed in Chap. 1 features control and readout as essential parts of any qubit. For superconducting circuits, an architecture known as circuit QED [5] realizes these processes via coupling to a superconducting resonator, as in Fig. 2b. The basic principle of circuit QED is that if a microwave frequency alternating voltage is applied, instead of static voltage V_g , transitions between qubit and resonator states can be driven. After the microwave voltage has passed through the circuit, the dependence of transmission on frequency can reveal information about the qubit state.

In circuit QED, the conventional type of resonator used is the transmission-line resonator, illustrated in Fig. 3a. This resonator is an isolated segment of metal fabricated on a chip by etching away contours between this segment and the surrounding ground plane. Similar to a regular cavity resonator, the resonant frequency f_R is determined by the length of the resonator. The quality of the resonator can be quantified by $Q_R = f_R/\kappa$, where κ is the photon decay rate; Q_R is called the resonator quality factor. A higher quality factor increases the coupling between

the resonator and qubit. In terms of circuit elements, the resonator can be thought of as an *LC* oscillator, with effective inductance L_R and capacitance C_R .

Circuit QED is a name adapted from the field of cavity QED within quantum optics. In cavity QED, the coupling between optical cavities and atoms is studied. In the circuit case, the optical cavity and atom is replaced by a resonator and a qubit, respectively, both fabricated in the solid state. The energy scales are vastly different, but the governing interaction has an identical structure, which is known as the Jaynes–Cummings Hamiltonian.

In the following, we describe a number of essential relations that are derived in Ref. 4. The coupled qubit–resonator system is described by the Jaynes-Cummings Hamiltonian \hat{H}_{JC} . In the basis of eigenstates $|i\rangle$ to \hat{H}_T of Eq. 6, the Hamiltonian of

$$\hat{H}_{JC} = \sum_n E_n |n\rangle \langle n| + hf_R \hat{a}^\dagger \hat{a} + \hbar \sum_{i,j} g_{ij} |i\rangle \langle j| (\hat{a}^\dagger + \hat{a}) . \quad (10)$$

where \hat{a}^\dagger and \hat{a} are ladder operators corresponding to adding and removing a photon from the resonator, f_R is the resonator frequency and g_{ij} is the coupling strength of the resonator to the qubit transition $|i\rangle \leftrightarrow |j\rangle$. In the transmon regime, Ref. 4 shows that

$$g_{j,j+1} \propto \sqrt{\frac{j+1}{2}} \quad (11)$$

and that all other (non-nearest-neighbor) couplings vanish as $E_J/E_C \rightarrow \infty$. For convenience, we refer to g_{01} simply by g in the following.

Using the circuit QED transmon system for quantum information processing necessitates operation in the strong dispersive regime, when

$$g \gg \max \gamma, \kappa \quad \text{and} \quad |\Delta| \gg g \quad (12, 13)$$

are satisfied, where γ, κ are the decay rates of the qubit and resonator, respectively, and Δ is the qubit–resonator detuning $E_{01}/\hbar - f_R$. In a spectroscopic sense, Eq. 12 (strong coupling) means that the anticrossing g between the qubit and resonator can be resolved despite the linewidths of both transitions. Eq. 13 (dispersive limit) means that the qubit and resonator transition frequencies are separated beyond hybridization, and is associated with effects enabling qubit-state readout. In Ref. 4, it is further shown that the Jaynes–Cummings Hamiltonian in the dispersive

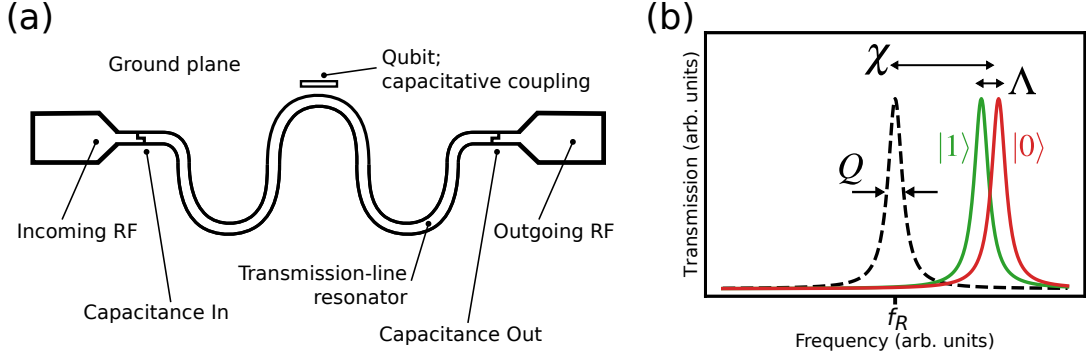


Figure 3: Circuit QED. (a) Schematic illustration of transmission line resonator coupled to transmon. (b) In the strong dispersive regime, the dependence of resonator frequency on the qubit state enables readout. Two distinct shifts, the dispersive Lamb shift χ and the qubit-state dependent shift Λ , are indicated in the plot. On the horizontal axis, f_R is the uncoupled resonator frequency.

regime is given by

$$\hat{H}_{JC} \simeq \frac{\hbar}{2} \left(f_{01} + \frac{g^2}{\Delta} \right) \hat{\sigma}_z + \hbar \left(f_R - \frac{1}{2} \frac{g_{12}^2}{\alpha/h + \Delta} + \left[\frac{g^2}{\Delta} - \frac{g_{12}^2}{\alpha/h + \Delta} \right] \hat{\sigma}_z \right) \hat{a}^\dagger \hat{a} \quad (14)$$

where the transition frequency $f_{mn} = E_{mn}/\hbar$, $\hat{\sigma}_z$ is the Pauli z -operator acting on the $\{|0\rangle, |1\rangle\}$ qubit subspace and higher-order qubit transitions have been taken into account before truncating to a two-level system. From the Hamiltonian on this form, it can be seen that two distinct shifts of the measurable resonator frequency is present. First, there is a qubit-state independent dispersive Lamb shift, due to the presence of the qubit coupling. Second, there is a qubit-state dependent shift. In the transmon regime $E_J/E_C \gg 1$, these shifts, as given by Eqs. 11 and 14, have the form

$$\chi = \frac{g^2}{\alpha/h + \Delta} \quad \text{and} \quad \Lambda = \frac{g^2}{h\Delta^2/\alpha + \Delta} \quad (15, 16)$$

where χ and Λ denote the dispersive Lamb shift and qubit-state dependent shift, respectively. The shifts are illustrated in Fig. 3b. In practice, when the qubit is operated in the dispersive regime, it is very often the case that $\Delta \gg \alpha/h$. Therefore, the presence of Δ^2 in the denominator of Λ means that (i) this shift is much smaller than the χ -shift and (ii) the direction of the Λ -shift is independent of the qubit state. Resolving the Λ -shift allows for readout of the qubit state.

In addition to reading out the qubit state by detecting a shift in the resonator frequency, the

qubit transition f_{01} can be directly driven by applying a microwave tone with this frequency. Quantum gates can then be applied by modulating such a tone in sequences of pulses with certain durations, which will be discussed further in Sec. 2.4. In combination with the readout procedure, this means that the circuit QED architecture offers a complete toolset for manipulating and measuring the coupled qubit.

2.1.3 Gate-tunable semiconductor nanowire transmon

Conventionally, the transmon JJs are Al–Al₂O₃–Al interfaces fabricated by oxidation of Al. This interface is an example of an S–I–S system, where S and I denote superconductor and insulator, respectively. The devices under investigation in the present project instead use a recently developed [13–15] S–Sm–S system, where Sm denotes semiconductor.

In this implementation, a semiconducting InAs nanowire with an Al shell is capacitively coupled to a transmission-line resonator. At low temperatures, the Al shell proximitizes the semiconductor nanowire, making it superconducting. Along a short segment in the middle of the wire, aligned with a bottom gate, the Al shell is etched away. By applying a static voltage to this gate, the Josephson energy E_J can be controlled *in situ*. For this reason, these gate-controlled devices are sometimes called “gatemons”. In traditional Al–Al₂O₃–Al devices, the E_J of individual junctions are fixed during device fabrication, and *in situ* control of an effective E_J is instead achieved by flux biasing a split-junction device. Electrostatic gates have several advantages compared to flux bias [13], one of which is enabling operation in a finite magnetic field, which is required for the Majorana experiments that are the topic of this thesis. Recent research [15] shows gatemons reaching coherence times (T_1 , T_2^*) on the order of 1–2 μs.

2.2 Majorana zero modes in solid-state systems

Majorana fermions are particles with the defining feature of being their own antiparticle. The fundamental Majorana fermions were introduced by E. Majorana in the 1930s. Decades later, extensive research on solid-state excitations with the same property is carried out worldwide, motivated in part by applications in quantum information processing. These solid-state quasi-particles are called Majorana zero modes (MZMs) detecting the presence of such an excitation

in a circuit QED system is the aim of the present project.

The particle–antiparticle property is expressed mathematically by $\hat{\gamma}^\dagger = \hat{\gamma}$, where $\hat{\gamma}^\dagger$ and $\hat{\gamma}$ denote the identical creation and annihilation operator of a MZM. Normal fermions, denoted by \hat{c}^\dagger and \hat{c} and obeying the anticommutation relation $\{\hat{c}^\dagger, \hat{c}\} = \delta_{mn}$, are complex superpositions of two MZMs;

$$\hat{c}^\dagger = (\hat{\gamma}_1 - i\hat{\gamma}_2)/2, \quad \hat{c} = (\hat{\gamma}_1 + i\hat{\gamma}_2)/2. \quad (17, 18)$$

and the fermionic number operators $\hat{c}^\dagger \hat{c}$ are the real observables of the physical system. Solid-state Majorana physics becomes interesting when two MZMs are spatially separated, together forming a delocalized fermionic state. This effect was first studied in a toy model by A. Kitaev [16]. The interacting particles in this one-dimensional Kitaev chain correspond to spinless fermions forming Cooper pairs with an unconventional symmetry (“*p*-wave”). The resulting spectrum of the Kitaev chain features a zero-energy fermionic state delocalized across the length of the chain or, in other words, a single MZM on either end of it.

Theoretical research later found a mapping of the Kitaev chain onto a realistic system composed of a conventional (“*s*-wave”) superconductor proximitizing a semiconducting quantum wire [17, 18]. The necessary components of the wire implementation are a semiconducting nanowire with large effective Zeeman *g*-factor and strong spin–orbit coupling, as well as a proximitizing superconductor, an in-plane magnetic field B_{\parallel} and a way to control the chemical potential of the wire, such as a gate voltage. This system is, if B_{\parallel} and V are correctly tuned, expected to enter the topological regime in which it hosts a MZM at each end of the topological segment. In 2012, Mourik *et al.* [7] reported signatures consistent with MZM presence in transport experiments implementing the wire scheme. These initial findings were supported by subsequent research, such as Ref. 19. In these experiments, the applied field required is on the order of several 100 mT to 1 T.

MZMs have an application in topological quantum computation (TQC) due to their non-abelian statistics [20]. The transformation of the quantum state of a system upon swapping the positions of two of its excitations is given by the exchange statistics of these excitations. The normal bosonic and fermionic exchange statistics are both abelian, which means that the order of particle exchanges does not alter the overall quantum state of the system. The non-

abelian statistics of MZMs, however, makes it possible to cast the system into different states by merely picking the order of particle exchange. This procedure is known as “braiding” and is how quantum gates are implemented in TQC. Braiding has yet to be experimentally realized.

TQC with MZMs consequently features two kinds of topological protections against decoherence: (i) by encoding the quantum state in a delocalized fermionic degree of freedom, the state is protected against local perturbations from the environment, and (ii) implementing gates by braiding MZMs, the operations alter the quantum state discontinuously, avoiding the loss of fidelity associated with rotating too short or too far with continuous gate operations.

2.3 Proposal for Majorana–transmon hybrid device

In order to facilitate the progress towards full TQC with braiding, as well as to complement the Majorana-compatible signatures reported from transport experiments, MZMs in various physical systems are being studied. The present project investigates experimentally a transmon system designed to host MZMs, which was introduced by Refs. 8, 21. The proposed device is referred to as Majorana transmon (MT) and the gatemon implementation we consider is illustrated schematically in Fig. 4a. The system consists of a gatemon qubit, similar to the one in Ref. 13, with additional large “plunger” gates intended to control the chemical potential in the wire. The gates are sandwiched between a bottom and top dielectric layer, in order to prevent leakage to substrate and transport through the nanowire, respectively.

If the superconductors on both sides of the transmon JJ are driven into the topological phase, by applying a magnetic field and tuning the chemical potential of the wire, MZMs appear at the ends of the topological segments. By making the length of the topological segments long enough, it can be assumed that there is no coupling between MZM pairs $\hat{\gamma}_1$ and $\hat{\gamma}_2$ or $\hat{\gamma}_3$ and $\hat{\gamma}_4$. However, the overlap of $\hat{\gamma}_2$ and $\hat{\gamma}_3$, introduces Majorana physics in the behavior of the device. These MZMs mediate coherent tunneling of single electrons across the JJ, described by the interaction \hat{H}_M , so that the total Hamiltonian \hat{H}_{MT} becomes

$$\hat{H}_{MT} = \hat{H}_T + \hat{H}_M \quad \text{and} \quad \hat{H}_M = iE_M \hat{\gamma}_2 \hat{\gamma}_3 \cos(\hat{\phi}/2) \quad (19, 20)$$

where E_M is the energy scale associated with the Majorana-induced single-electron tunneling.

The factor $1/2$ in the cosine is directly related to the electron charge $1e$ compared to the Cooper pair charge $2e$. The magnitude of E_M is unknown but can be measured in a realization of the MT. This measurement would provide useful information about Majorana effects in superconducting circuits and is one of the key goals of the present project.

A numerical diagonalization of \hat{H}_{MT} yields the energy level diagram in Fig. 4b. As discussed in Sec. 2.1.1, quasiparticle poisoning effectively (for measurements slower than the poisoning timescale) causes an overlap of $1e$ -offset parabolas for a regular transmon. For the MT, however, these double parabolas are inherent in the energy spectrum and the parabolas anticross instead of crossing. This anticrossing in the charge dispersion provides a clear MZM signature, detectable in a circuit QED architecture. By measuring the size of this anticrossing, E_M can be induced. Furthermore, the individual transitions are split due to the availability of additional transitions; however, the splitting is into two lines and not four, since the coupling between transitions between states of different parity is vanishing [8].

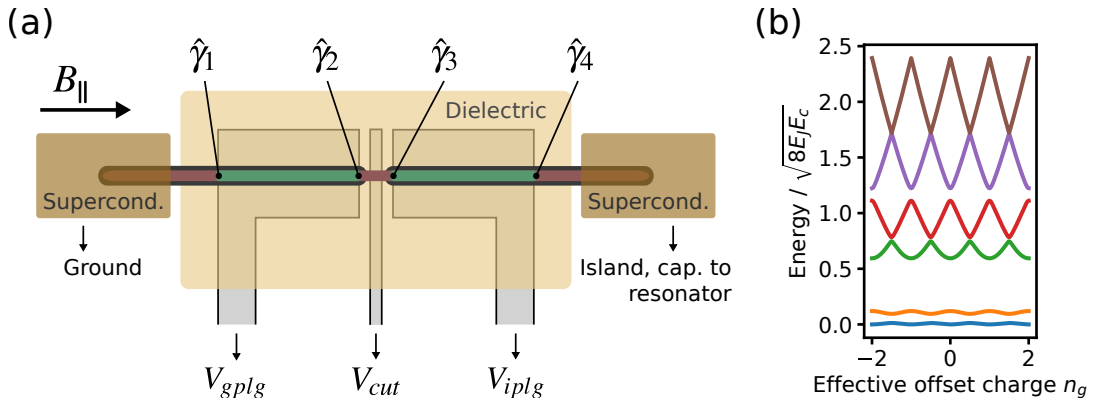


Figure 4: Majorana–transmon implemented in a proximitized semiconductor nanowire. (a) Schematic illustration of MT device to be implemented in the present project. Two segments of a proximitized semiconductor nanowire are driven from the trivial (red) into the topological (green) regime by an in-plane magnetic field $B_{||}$. (b) MT energy level diagram. In this example, $E_J/E_C = 2$ and $E_M/E_C = 1/5$. Calculations performed using code from Ref. 22.

An alternative approach, also pursued experimentally in the present project, is split-junction geometry devices. In this geometry, the nanowire is contacted also at its midpoint, and two duplicate JJs and plunger–cutter–plunger gate sets are located on either side of this mid-

dle contact. The middle contact is connected to the superconducting island and the outer ones to the ground plane, forming a SQUID-type loop. As mentioned in Sec. 2.1.3, split-junctions in normal transmons introduce a flux-dependence of the Josephson energy according to $E_J = E_{J,\max} |\cos(\pi\Phi/\Phi_0)|$ [4] which implies periodic flux dependence of the qubit frequency $f_{01} \propto \sqrt{E_J}$.

In an applied magnetic field, the system can enter a topological phase. For the split-junction geometry, this means that eight MZMs are present and coherent single-electron transport can take place across both JJs. Numerical calculations [22] show that the magnetic flux dependence becomes “ 4π periodic” in the manner showed in Fig. 5. Note that in this figure, energy differences are directly plotted, corresponding to a spectroscopically measurable spectrum. Accordingly, an MZM signature for the split-junction MT is an E_M -induced splitting of the transition frequency, occuring every other period in the magnetic flux dependence.

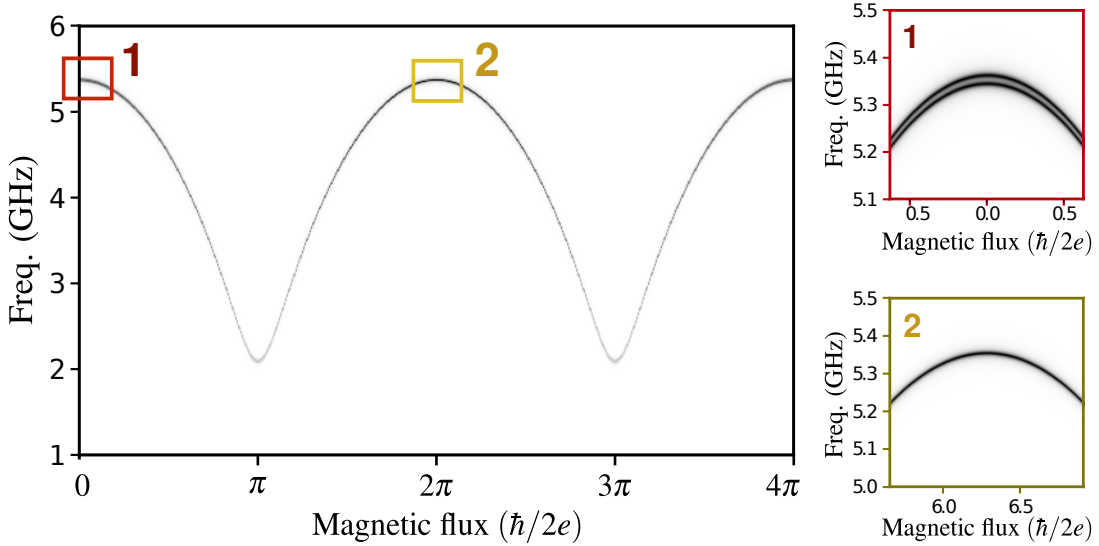


Figure 5: Numerically calculated transition spectrum of split-junction Majorana transmon for the parameter values $E_C/h = 230\text{ MHz}$, $E_J/h = 10\text{ GHz}$ for one junction, $E_J/h = 7\text{ GHz}$ for the other junction and $E_M/h = 100\text{ MHz}$ for both junctions. (The E_C and E_J parameters are similar to typical experimental values. The experimental value of E_M is unknown.) A 4π periodicity in the flux dependence is introduced by the presence of Majorana zero modes. Calculations and adapted figure from Ref. 22.

2.3.1 Aspects of physical realization

In order to adapt the nanowire qubit described in Sec. 2.1.3 to the MT implementation, a number of considerations have to be made. In this section, some of these aspects are presented.

The gatemon described in Sec. 2.1.3 uses a nanowire with a shell covering the full circumference of the wire. This is not suitable for the MT case, since the shell would screen the potential from the plunger gates, needed to tune the device into the topological regime. For this reason, “half-shell” wires with Al deposited only on 2 or 3 out of the 6 hexagonal facets are used for the devices in this project.

Another important aspect is the need to apply a large magnetic fields to drive the junction into its topological regime. Since the qubit and surrounding architecture is entirely based on superconductivity, this presents a problem. The resonator film can not, for example, be fabricated in Al due to its low $B_c \sim 10\text{ mT}$. The superconducting material used is instead NbTiN, which is known to have a large B_c , sufficient for the MT experiment. A potential source of microwave losses and qubit decoherence is magnetic flux noise, which can result from flux quanta moving around between different features on the sample. By fabricating large arrays of holes in the resonator film, these vortices can be trapped, reducing noise and increasing the quality factor of the resonator. These holes are referred to as flux-trapping holes. The high-field compatible NbTiN resonators used in this project were developed by Ref. 23. As for other material choices, the standard substrate material Si is used and the dielectric is chosen to be HfO_2 due to availability in the processing facilities and positive experience in similar experiments.

Typically, the incoming and outgoing microwave connections on the sample are located at the edge of the chip. This means that the resonator splits the ground plane of the chip into multiple parts, which can be associated with standing waves in the sealed-off areas, reducing the resonator Q . To avoid this, the two sides of the resonators can be electrically connected using metallic bond wires. However, the applied field can make these bond wires turn normal, which by the superconducting proximity effect can also affect the other parts of the circuit. This is a problem in particular if these bond wires are located close to the qubit. Therefore, a construction with NbTiN bridges on top of crosslinked (insulating) resist is used in place of these on-chip bond wires.

In practice, a given sample loaded into the measurement setup typically features more than one qubit. These qubits can either all be coupled to a single resonator or to individual resonators, probed via a common feedline. In this project, both approaches have been used.

2.4 Qubit coherence and manipulation

The coherence times are fundamental properties of a qubit implementation, indicating the timescale during which the system can be expected to remain in a well-defined state (corresponding to a point on the Bloch sphere). The relaxation time T_1 is a measure of the time before a qubit state $|1\rangle$ decays into a $|0\rangle$ state. In such a decay, the energy level spacing of the states is transferred to the environment that the qubit is coupled to. For this reason, isolating the qubit makes it more long-lived; doing so, however, makes readout harder to achieve. In addition to relaxation, noise from the environment causes the effective Hamiltonian of the qubit to fluctuate, resulting in dephasing of the qubit state. The dephasing timescale timescale is denoted by T_2^* .

By driving transitions in pulses, the coherence times of a qubit device can be measured. The pulse sequences are illustrated in Fig. 6 and described below. In general, a pattern of qubit operations are applied, after which the state is read out. In the case of circuit QED, the operations are performed by pulsing the qubit frequency, and readout by applying a resonator-frequency tone and observing the shift of the transmitted signal. As the readout tone is applied, the qubit state is quantum mechanically collapsed into either $|0\rangle$ or $|1\rangle$. In order to infer the z -axis projection K_z of the state (prior to the measurement) many measurements must be performed, which are then averaged to produce a probability.

In a Rabi experiment, a qubit-frequency microwave pulse of variable length drives the $0 \leftrightarrow 1$ transition, which is also known as inducing Rabi oscillations between the states. As the qubit state decoheres, which can be represented by the Bloch sphere radius shrinking, the oscillations dampen into the midpoint superposition of states. From the periodicity of Rabi oscillations, the π -pulse duration t_π can be extracted.

It can be demonstrated (see e.g. Sec. 7.3 of Ref. 24) that the frequency of the Rabi oscillations has a quadratic dependence on small offsets between the driving microwave frequency

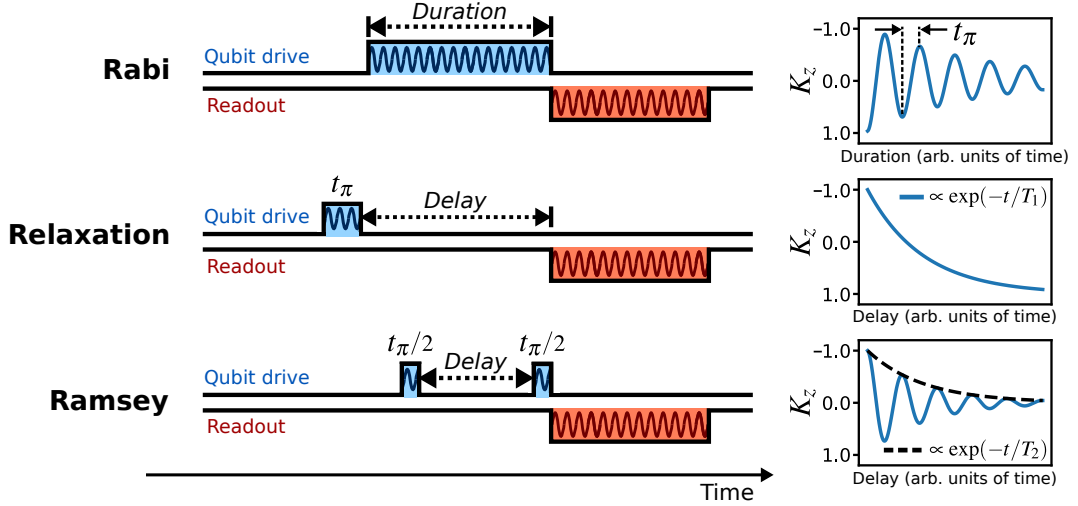


Figure 6: Pulse sequences for time-domain qubit experiments. To the right, plotted curves of mock measurement results illustrate how qubit properties are extracted from the experiments. For each sequence, the dotted arrow corresponds to the independent variable in the plot.

and the qubit transition frequency. Measuring Rabi oscillations as a function of drive frequency, around the qubit frequency, produces a characteristic two-dimensional pattern, indicative of coherence and stability of the qubit.

The relaxation experiment consists of exciting the qubit to the $|1\rangle$ state by applying a qubit-frequency pulse of length t_π . The system is then left to evolve during a variable delay after which it is read out. After many measurements, fitting the decay of K_z to an exponential function (the expected functional form), the relaxation time T_1 can be determined.

In order to probe the dephasing time T_2^* a Ramsey experiment is used. Here, qubit state is excited down to the Bloch sphere xy -plane (“equator”) by application of a qubit-frequency pulse of length $t_\pi/2$. After a variable delay, another $t_\pi/2$ is applied. By fitting an exponential envelope to sinusoidal oscillations, T_2^* is determined.

Chapter 3 Experimental method

3.1 Fabrication of qubit devices

Fabrication of the qubit devices in the present project is achieved by standard integrated-circuit (IC) fabrication methods and has been carried out in the Niels Bohr Institute cleanroom facilities. The fabrication methods used are very well-developed and are described in detail e.g. in Ref. 25. Before fabrication, the devices are designed in CAD software, and numerical simulations predict features such as the resonator frequency, its quality factor and the charging energy E_C of the superconducting island.

Lithographic patterns are written using electron beam lithography (EBL). In EBL, a beam of electron exposes pattern in resist, which can then be used for selective metallization. The EBL technology can achieve nanometer-scale resolution. In principle, it can be said that there are two different ways to create patterned metal regions on the sample: (i) the lift-off procedure, where a pattern in the resist is created (by deposition, exposure and development), metal is deposited globally and the unwanted metal is lifted off by stripping the resist; (ii) the etch-back procedure, where metal is first deposited globally, and patterned resist on top of it is used to selectively etch away the unwanted metal.

The typical processing sequence, relevant for all devices in the thesis, is outlined below. Fabrication of all devices has been performed on 2 inch diameter Si wafers grown along the $<100>$ crystal axis. The wafers have a nominal room temperature resistance above $5\text{ k}\Omega$ and the conductance is expected to be negligible at the fridge base temperature. The first processing step is creating metal alignment marks in a lift-off procedure. After this, the bottom dielectric area is deposited using lift-off and atomic layer deposition (ALD). By sputtering in an etch-back procedure, the 20 nm NbTiN resonator-layer film is fabricated. The etched pattern contains the resonator, gates and lines connecting them. In addition, the gate lines feature on-chip low-pass *LC* filters, based on work in Ref. 26. In the sputtering step, the sample is bombarded with Nb and Ti in an environment of N, configured such that NbTiN is formed on the surface. Next, the top dielectric area is deposited in the same type of procedure used for the bottom one.

After these steps, individual nanowires are deterministically deposited on the dielectric area using a micromanipulation system and resist is then spun on, keeping them in place. The wires are grown by collaborators [27] using a VLS technique. Etch windows patterns are then written by EBL over the junction gate, so that local wet etch of Al then can be performed, forming the weak link between the superconductors. Following the etch, NbTiN contacts are deposited by sputtering in a lift-off procedure. In parallel with the above steps, the on-chip crossovers consisting of crosslinked PMMA and NbTiN are also fabricated.

Individual samples for insertion in the sample holder of the dilution refrigerator are cut out using a dicing saw. These smaller samples are then wire bonded to a PCB suited for the sample holder. Inspection by scanning electron microscopy (SEM) is performed either before or following measurement in the dilution refrigerator.

3.2 Measurement setup with dilution refrigerator

The characterization and microwave measurements of the devices are performed in a dilution refrigerator. The full circuit of the measurement setup¹ and its division into regions at different temperatures is schematically represented in Fig. 7. For operation, the instruments are connected to an acquisition PC via GPIB and LAN connections. The setup can be thought of as operating in one of two different modes, depending on the state of the switch. If the switch is turned to the left (time-domain mode) the RF sources modulated by an arbitrary waveform generator (AWG) send microwave pulse sequences down to the sample, and the transmitted signal is measured by the digitizer. With the switch turned to the right (spectroscopy mode), continuous-wave measurements are performed with the vector network analyzer (VNA).

In the time-domain configuration, the transmitted microwaves are measured by a digitizer at a lower frequency. In a mixer component, the transmitted signal is multiplied with a local oscillator RF source set to a frequency detuned from the cavity source by around 20 MHz. The output of the mixer will contain one component corresponding to the incoming difference and one to the sum; out of these components, the former is isolated by low-pass filtering. After

¹The device which has its results presented in Sec. 4.1 was measured in a slightly different, but qualitatively similar, setup.

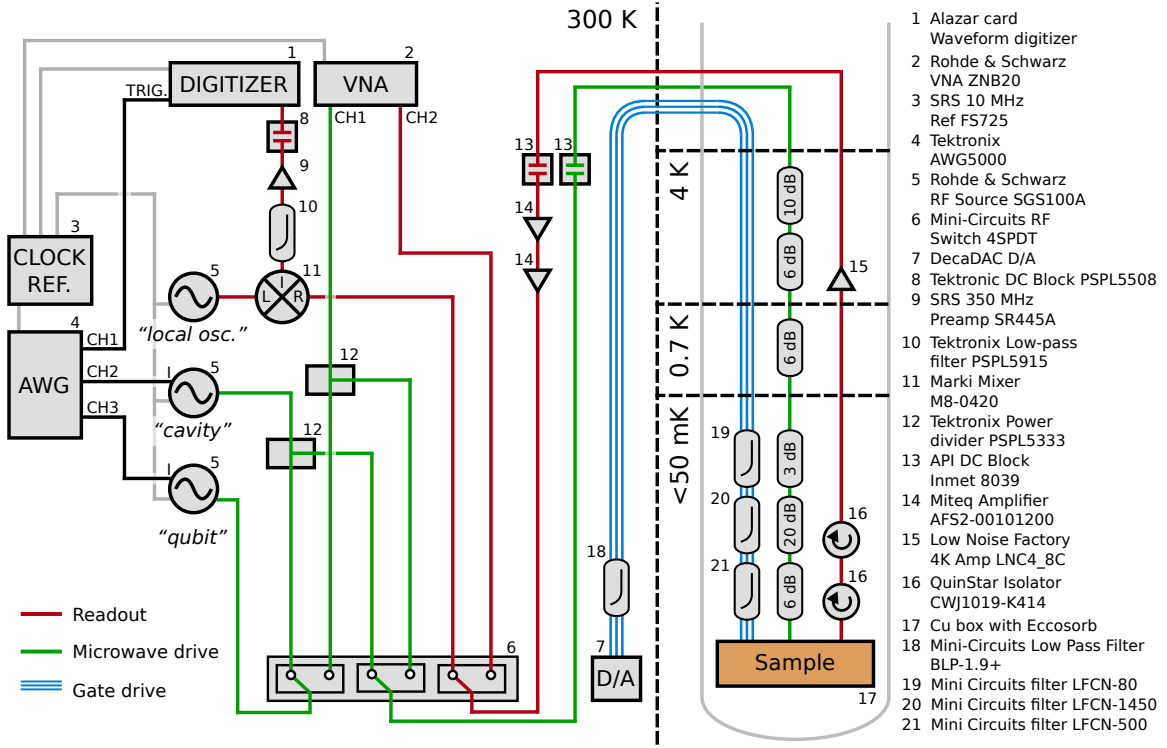


Figure 7: Full schematics of the measurement setup. Black dashed lines separate regions of different temperature. The gray can shape represents a dilution refrigerator. Not included here is additional filtering on the gate drive lines inside of the Cu sample box and on the PCB. Based on figure in Supplemental Material of Ref. 14.

having been sampled by the digitizer, the signal undergoes a digital downconversion process, resulting in a static voltage V_T , which is what is measured for transmission. This detection scheme is known as heterodyne readout.

Dilution refrigeration works by exploiting differences in the quantum mechanical nature of the two helium isotopes ^3He and ^4He . The technology has been in existence since the 1960s and is described in detail e.g. in Chap. 7 of Ref. 28. To achieve cooling, a ^3He – ^4He mixture is first cooled down below 1 K, where they phase separate into a ^4He -rich phase with 6.6 % ^3He and a ^3He -rich phase with a very small amount of ^4He . By pumping on the ^4He -rich phase, the diluted ^3He is extracted in a distillation chamber (“still”). This is balanced by ^3He in the ^3He -rich phase crossing the phase boundary, which constitutes the source of cooling power. The cooling is supplied at the phase boundary, which is located in a vessel called the “mixing

chamber” (MC). In the setup of the present project, the MC reaches temperatures of 30–40 mK. In order to perform low-temperature experiments, samples are loaded into the refrigerator and positioned at the MC.

3.3 Procedures for qubit characterization

In this section, the basic measurement procedures that were used for qubit characterization are listed and briefly described.

- **Resonator power shift (qubit presence).** As an initial measurement, studying the power dependence of the resonator peak gives an indication whether the device fabrication was successful. The resonator shifting away from its bare value at low power likely means that the presence of the qubit is causing a dispersive shift.
- **Two-tone spectroscopy.** In order to spectroscopically probe the qubit via the resonator, a two-tone measurement is performed. With the readout frequency set to on a point of maximal slope on either side of the resonator, the frequency of the *qubit* RF source is swept. If the swept frequency becomes resonant with the qubit transition, it will drive this transition, causing a qubit-state dependent resonator shift (Λ -shift) which will result in a signal in the transmitted readout microwaves. Two-tone spectroscopy can be used for tracking the qubit transition as a function of other parameter, such as a gate voltage or applied magnetic field. If the qubit transition is driven at high enough power, multi-photon processes become visible in the spectrum, i.e. transitions at twice energy of the applied frequency will shift the resonator. These features, such as $f_{02}/2$, provide a good indication of transmon behavior.
- **Time domain measurements.** The typical procedure that has been used to characterize the coherence of the qubit is described in the following. First, the qubit f_{01} frequency is determined by a wide scan in spectroscopy mode from which the relevant extremum frequency is extracted. The setup is then turned to time-domain mode and a set of time-domain experiments (Rabi, relaxation, Ramsey; the latter two using t_π obtained from the first) is performed with the qubit drive set to f_{01} .

Finally, it is important to mention that in order to enhance the visibility of the relevant signals in spectroscopic measurements, the average voltage from each sweep of drive frequency can be subtracted from all points in the corresponding row. This is done after the measurement has been performed. The majority of spectroscopic data sets presented in Sec. 4 have been processed in this manner.

Chapter 4 Results

4.1 Single-junction qubit designed for $E_C/h = 230\text{MHz}$

The geometric design of this device was made by Thorvald Wadum Larsen. Initial fabrication from blank Si wafer was performed by Marina Hesselberg and Robert McNeil. I performed fabrication starting from nanowire deposition. I assisted Thorvald Wadum Larsen in performing the microwave measurements.

Micrographs of this device are displayed in Fig. 8. After having been loaded in into the measurement setup, initial power-dependence transmission measurements indicated a coupling between the resonator and a qubit, due to a splitting of the resonator at low power. The sample was fabricated to feature two nanowire qubits, one of which ($Q1$) without the plunger gates described in Sec. 2.3 and the other one ($Q2$) with the plunger gates present. Only the $Q1$ cutter gate had an effect on the resonator frequency in the transmission measurement; for this reason, only $Q1$ was studied in further measurements.

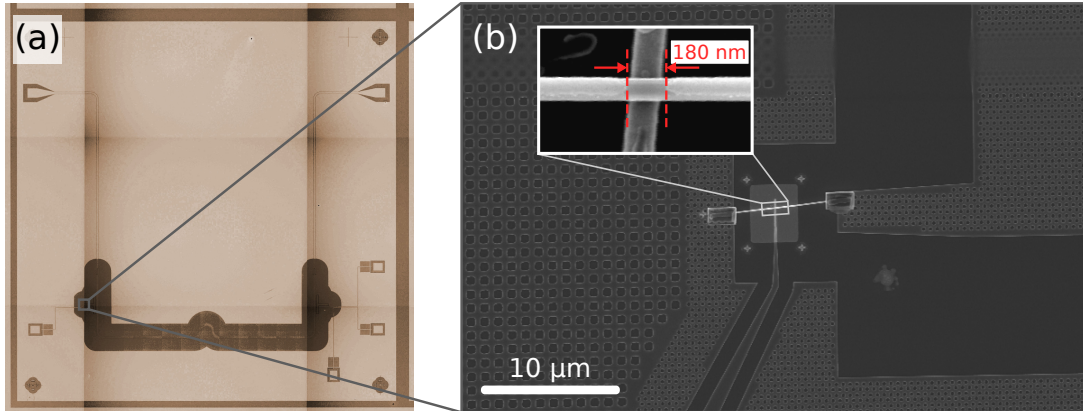


Figure 8: Single junction $E_c/h = 230\text{MHz}$ qubit. (a) Optical micrograph of full chip. Two nanowire qubits were fabricated on the chip; measurements on the leftmost one are included in the present thesis. (b) Scanning electron micrograph showing the nanowire and its junction gate. In the inset, a micrograph with increased magnification shows that the Al facets have been etched away over a 180 nm segment.

The bare resonator frequency was measured to be 7.999 GHz. Wide spectroscopic two-tone

measurements revealed the qubit frequency, and a power-dependent spectroscopic measurement was performed, see Fig. 9. An anharmonicity α/h of 18 MHz was measured. In Fig. 9b, results from a wide sweep of the cutter gate are displayed, revealing a nonmonotonic dependence of the qubit frequency, tending to increase with the cutter voltage.

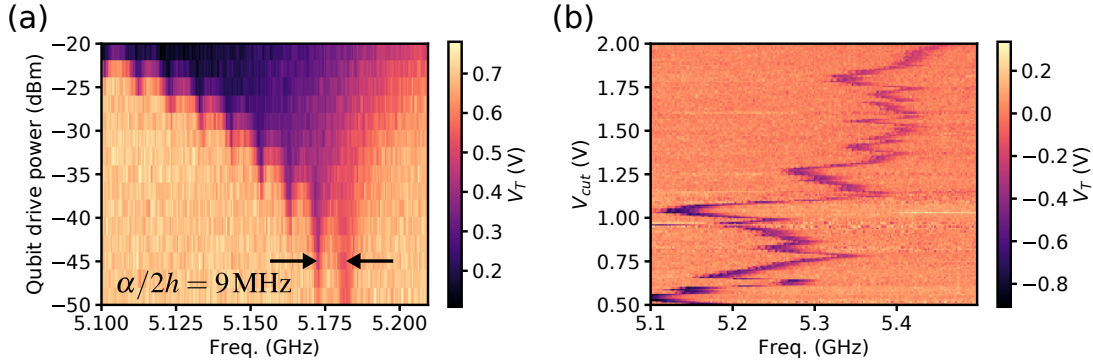


Figure 9: Zero field characterization of $E_C/h = 230\text{MHz}$ qubit. (a) Power dependence experiment, revealing several multiphoton processes corresponding to higher-order transitions. (b) Dependence of the qubit transition frequency on the voltage of the cutter gate at the JJ.

Following the initial characterization at zero magnetic field, the vector magnet was ramped up in a stepwise manner. These results of these measurements are shown in Fig. 10. During the ramping of field magnitude, relaxation experiments in the time domain were performed at certain field magnitudes. Before any signatures of MZMs were observed, the qubit transition disappeared from the spectroscopy at approximately 130 mT (Fig. 10b).

4.2 Single-junction qubit designed for $E_C/h = 500\text{MHz}$

For this sample, Anders Kringhøj performed the geometric design. The initial fabrication starting from blank wafer was performed by Marina Hesselberg and Robert McNeil. I performed fabrication starting from the Al wet etch. Me and Anders Kringhøj together performed the microwave measurements.

Images of the finished device are displayed in Fig. 11. The chip features four different qubits with differently sized islands, for different charging energies E_C . In the sample geometry, each qubit is coupled to a dedicated resonator. All the resonators are connected to a common feedline,

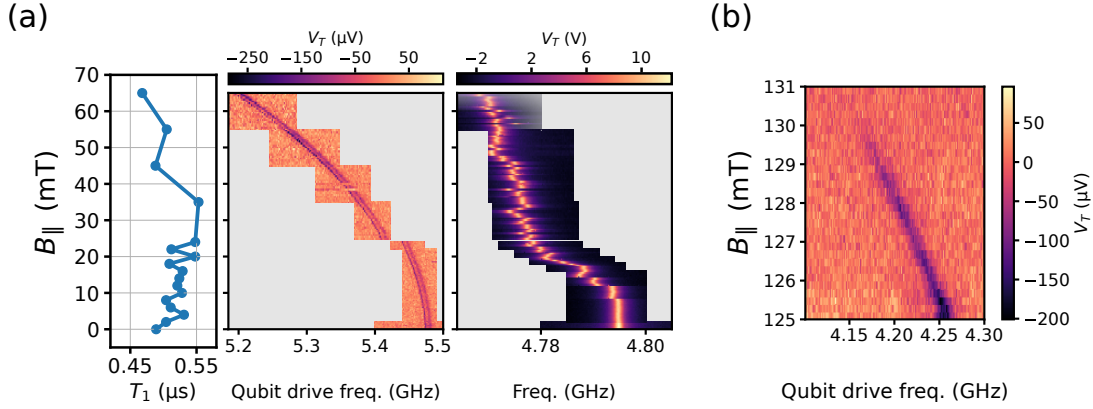


Figure 10: Increasing the parallel magnetic field of the $E_C/h = 230$ MHz qubit. (a) Dependence of qubit relaxation time (T_1) at different points of magnetic field. (b) Qubit transition frequency disappearing from spectroscopy as the magnetic field is increased.

through which microwave tones are applied. Initial measurements revealed that only a single qubit, with $E_C/h = 500$ MHz, was operational.

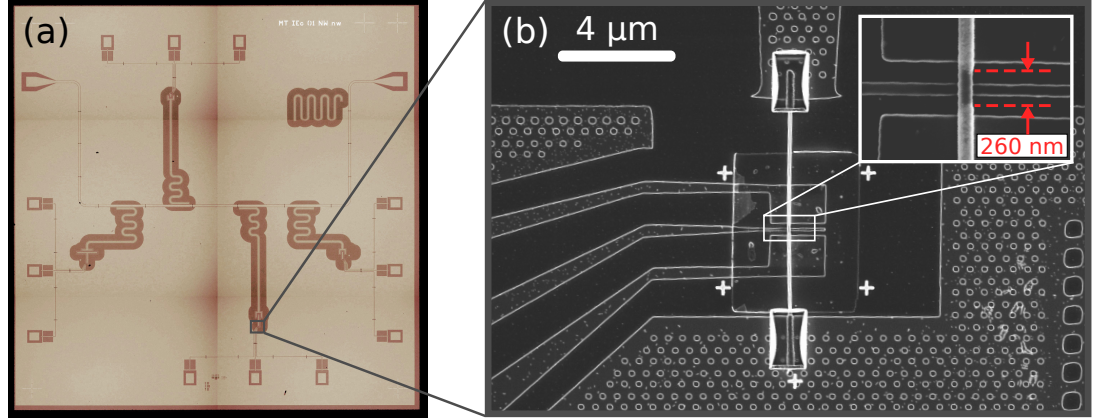


Figure 11: Single-junction $E_C/h = 500$ MHz qubit. (a) Optical micrograph of full chip, featuring the qubit as well as three other similar devices. (b) SEM image of the $E_C/h = 500$ MHz device.

A power-dependent scan revealed a qubit–resonator coupling and the bare resonator frequency of 5.850 GHz. At zero magnetic field, power and gate dependence microwave measurements were performed. The results of these measurements are displayed in Fig. 12; it was found that $\alpha/h = 160$ MHz and the qubit transition frequency could be controlled using the cutter gate.

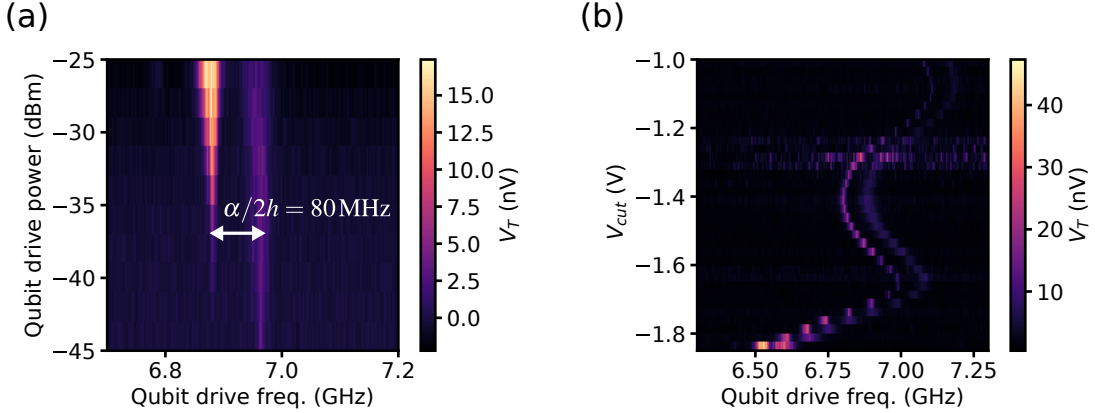


Figure 12: Zero-field measurements of $E_C/h = 500 \text{ MHz}$ device. (a) Power dependence, showing the $0 \leftrightarrow 1$ transition and two-photon $0 \leftrightarrow 2$ transition. (b) Gate control of the transition frequencies.

The magnetic field was increased while spectroscopically monitoring the qubit and performing time domain measurements; results are shown in Fig. 13. Time domain measurements for both the relaxation time T_1 and dephasing time T_2^* were performed up to 70 mT. At $B_{\parallel} = 20 \text{ mT}$, a drive-frequency-dependent Rabi measurement was performed, the results of which is clearly showing the characteristic quadratic pattern, indicating that the qubit is stable in time (Fig. 13b).

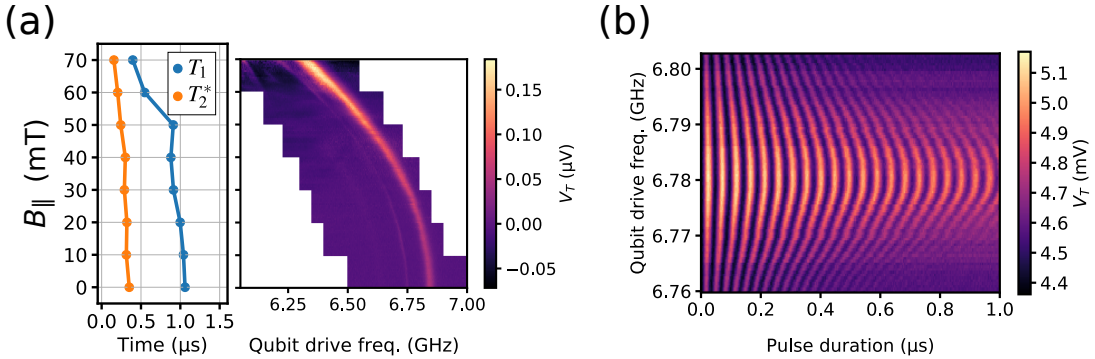


Figure 13: Magnetic field ramping for $E_C/h = 500 \text{ MHz}$ qubit. (a) Qubit frequency and coherence times as function of in-plane field. (b) Rabi measurement at 20 mT for different drive frequencies, centered around the qubit frequency.

Having reached $B_{\parallel} = 160 \text{ mT}$, the gate dependence of the qubit was measured again, see Fig. 14. In a plunger gate measurement, charge dispersion of the (two photon) $0 \leftrightarrow 2$ transitions could be resolved, showing crossings (not anticrossings) between the $1e$ offset gate voltage peri-

odic transitions. In a wider cutter gate sweep (Fig. 14b), an unknown mode was seen to approach and anticross with the qubit $0 \leftrightarrow 1$ transition. Observations of unknown modes interacting with the qubit at high magnetic fields have been made also in similar parallel experiments, not reported in the present thesis. After increasing the field further, the qubit transition disappeared from spectroscopy at around 200 mT.

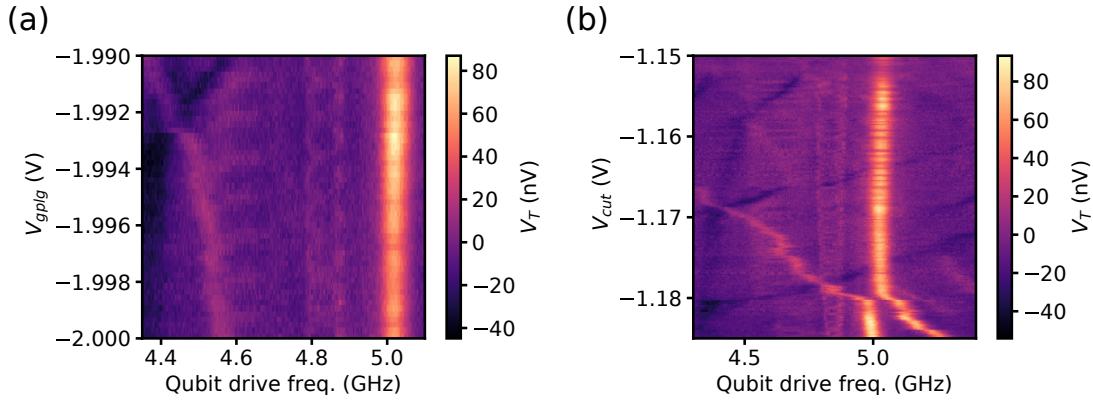


Figure 14: Spectroscopic gate dependence measurements of the $E_C/h = 230\text{MHz}$ qubit at $B_{\parallel} = 160\text{mT}$. (a) Charge dispersion of qubit energy levels. (b) The qubit frequency f_{01} anti-crossing with an unknown mode on the chip.

4.3 Split-junction qubit device

Thorvald Wadum Larsen made the geometric design of this device. All of the fabrication was performed by Marina Hesselberg and Robert McNeil. All measurements were performed by me.

The finished device inspected in microscopy is displayed in Fig. 15. Apart from the split-junction qubit, this sample also featured a gatemon qubit for reference. Initial measurements revealed that this gatemon seemed not to show up in measurement, indicating a fabrication failure.

The results of the characterization at zero magnetic field is shown in Fig. 16, with the bare resonator frequency measured to be 6.964 GHz. Several higher-order transitions were observed in a power dependence measurement, and the qubit frequency could be controlled using either junction cutter gate. The absolute anharmonicity α/h was measured to be 114 MHz.

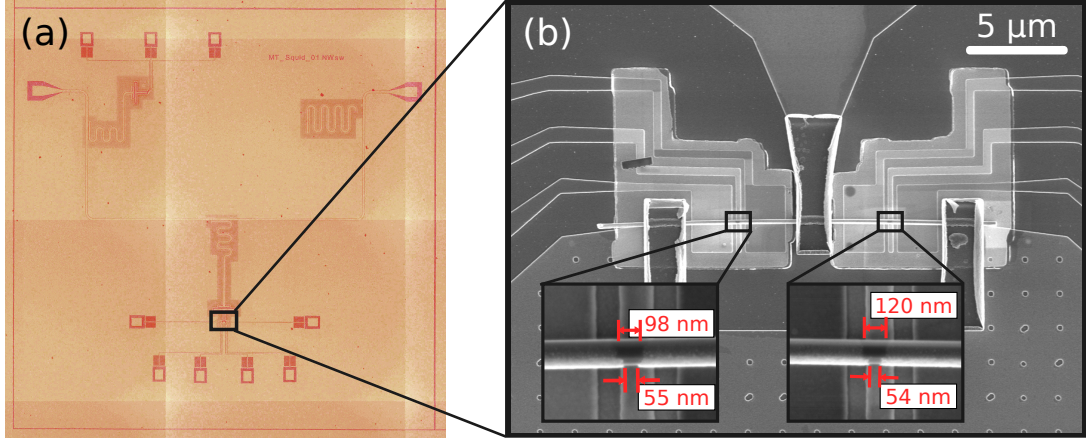


Figure 15: Micrograph of split-junction device. (a) Optical micrograph of sample featuring the device, as well as a standard gatemon qubit (top left corner). (b) SEM image of split-junction with etch widths highlighted.

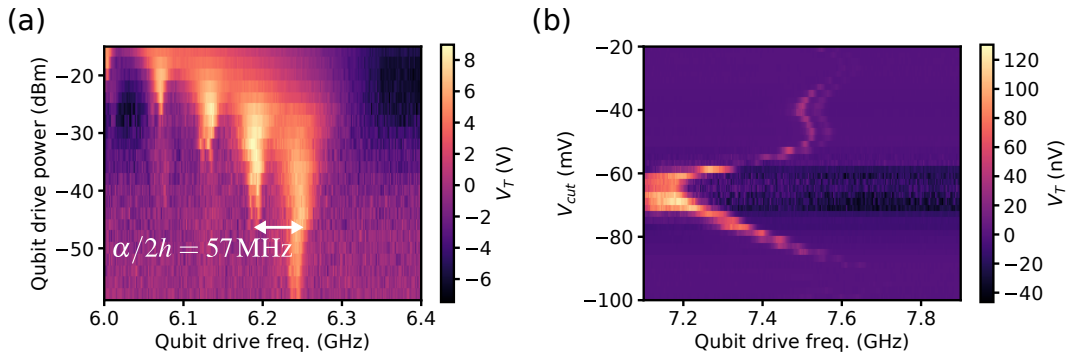


Figure 16: Zero field measurements of split-junction device. (a) Power dependence of qubit transition frequencies. Several higher-order transitions can be observed at high drive power. (b) Gate control of qubit frequency.

For this device, the magnetic-flux dependence could be used for aligning the magnetic field. From small changes in the angle specifying the out-of-plane component of the magnetic field, the flux dependence was suppressed for a certain angle, which was then used to define B_{\parallel} . The measurement results from this procedure are displayed in Fig. 17. A number of time domain measurements at zero field was performed. In one of these sets of measurement, a relaxation and Ramsey experiment revealed $T_1 = 720 \text{ ns}$ and $T_2^* = 31 \text{ ns}$, respectively, with the qubit frequency at 5.689 GHz.

In order to search for the MZM signature in flux dependence, the parallel field B_{\parallel} was in-

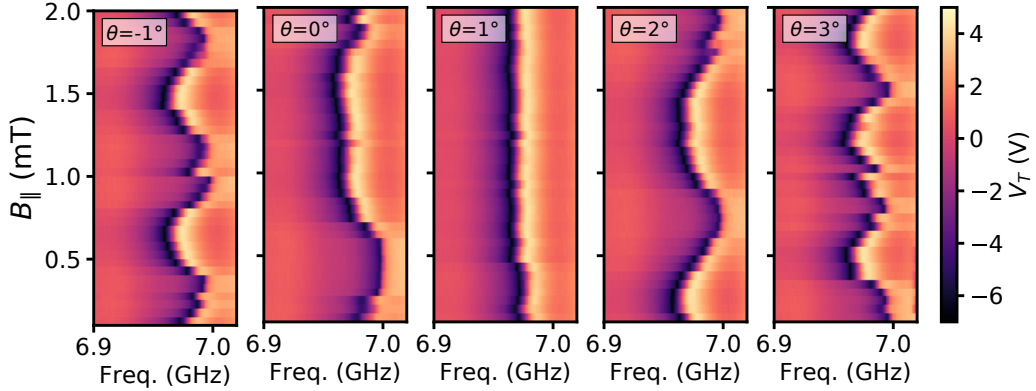


Figure 17: Field alignment using SQUID. The angle θ defining the magnitude of the component of B_{\parallel} nominally out of the chip plane is varied, and the orientation is picked so that the flux dependence is suppressed (here $\theta = 1^\circ$).

creased. Every 100 mT, the ramp was interrupted and the perpendicular field B_{\perp} was swept by 50 μ T. These measurement results are shown in Fig. 18. In addition, time domain measurements were also performed between these increases in B_{\parallel} . At 100 mT, the relaxation time T_1 was measured to be 114 ns. At 200 mT and 300 mT, no signal was observed in time domain measurements. At larger magnetic fields, no time domain measurements were performed. After losing the signal at $B_{\parallel} = 0.5$ T, some actions were attempted in order to possibly recover the spectroscopic peak. These actions included setting the gates to different voltage configurations, and increasing the field further (up to 1 T). None of these actions recovered the spectroscopic signal.

Furthermore, it was observed that the flux dependence of the qubit frequency was suppressed by setting the cutter gate of either junction to a large negative value; sweeping the perpendicular field B_{\perp} by 50 μ V with the left $V_{cut} = -1.4$ V, no change in the qubit frequency was observed. In this configuration of the left JJ depleted, a set of time domain measurements at zero field gave the results $T_1 = 166$ ns and $T_2^* = 304$ ns (qubit frequency 5.948 GHz).

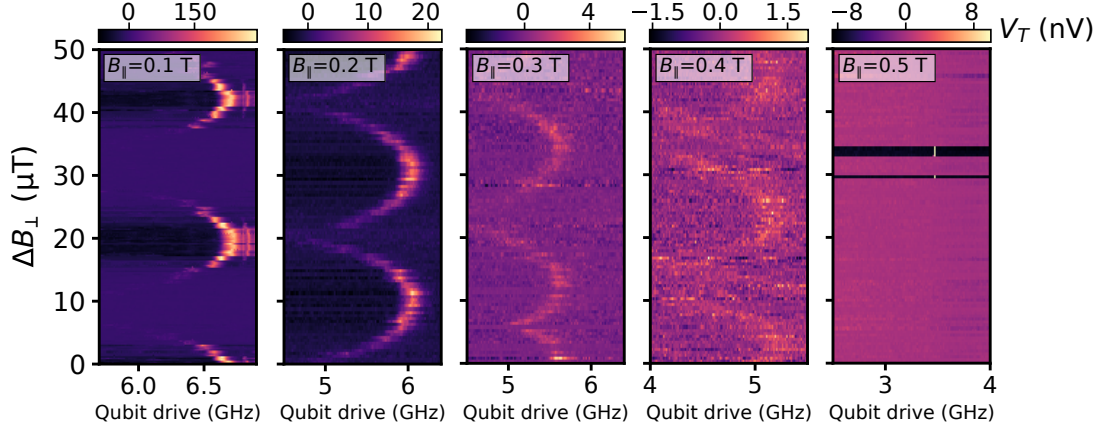


Figure 18: Magnetic flux dependence of split-junction device at different values of the in-plane magnetic field B_{\parallel} .

Chapter 5 Discussion

Although several devices were successfully fabricated and microwave measurements indicated the presence of qubits with expected behavior, the results presented in the previous section do not reveal any MZM signatures. For all devices, the failure is related to losing the qubit signal when the applied magnetic field is sufficiently large, before reaching a regime where signatures are expected.

For the device in Sec. 4.1, the anharmonicity measured at zero field is very low compared to the expectation from the transmon expression in Eq. 9. For the purposes of quantum information processing, this is a negative outcome, since low anharmonicity could result in leakage to higher states when driving the $0 \leftrightarrow 1$ transition. Unexpectedly low gate mon anharmonicity has been encountered before and attributed to a low number of conduction channels [15]; the deviation here is however larger.

There are two interesting things to note about the results in Fig. 10a. First, the qubit transition frequency as a function of field follows a smooth dependence on the applied field while the resonator frequency seems much less stable in the field. This is useful to know because it indicates that the circuit QED qubit–resonator system can reveal stable qubit features even if the resonator is not as stable in magnetic field, so there is not necessarily a need e.g. to optimize the fabrication for such a resonator stability. Second, the relaxation time T_1 , over the range

it is was measured (several tens of mT), seems fairly constant as a function of field. Despite the outcome of the MZM signature search ultimately being negative, the fact that coherence of these superconducting qubits can remain in field for some extent provides hope for continued research.

A better agreement with the transmon formula for anharmonicity in Eq. 9 is displayed in the results of measurements in zero magnetic field for the device presented in Sec. 4.2 (Fig. 12). For this device, the situation seems more comparable to Ref. 15. In the light of the results in Fig. 13a, this indicates that we are able to take a device resembling a conventional gatemon into magnetic field, while preserving coherence at least up to 50 mT. In the results in Fig. 14a, charge dispersion, the relevant spectroscopic effect for detecting MZMs in these systems, is resolved at 160 mT. The resolved charge dispersion is in the 2-photon f_{02} transition. In order to provide a convincing demonstration, the f_{01} charge dispersion should arguably also be resolved. Nevertheless, it is encouraging that the detection measurement could be performed at a field approaching those relevant for entering the topological regime (0.5–1 T). The reason why the qubit transition then vanished at a slightly larger field is not clear (this is also true for the previous single-junction device discussed above).

The split-junction device results, presented in Sec. 4.3, presents an alternative approach to detection of MZMs in circuit QED systems. The coherence, gate control and anharmonicity (Fig. 16) demonstrates that this alternative device works according to the expectations from a single-junction gatemon. As seen in Fig. 18, however, the spectroscopic signal vanishes at large magnetic fields. The fact that its visibility does persist up to 300 mT (arguably to 400 mT) puts it close to the necessary fields. The cause of the signal loss could be related to magnetic flux noise becoming more severe in a large magnetic field. It was also observed that nearby magnets could affect this device, indicating that it might need further shielding from the environment.

In summary, while none of the signatures searched for were observed in the devices, the results constitute a demonstration of the operation of gatemon qubits compatible with MZMs. The information about the behavior of the devices measured in this project could guide future research on similar systems.

5.1 Outlook

In terms of suggestions for further pursuing the research presented in this thesis, a number of specific and more general points can be made. The single-junction experiment could still be re-attempted; data from more devices could provide more insight to the general behavior of the type of device. Furthermore, more carefully studying the dependence of e.g. coherence times on fabrication parameters could provide useful insights, even if not directly related to signatures of MZMs.

The loss of signal in the split-junction device could potentially be mitigated by extending the setup to include some form of magnetic shielding. Another immediate option is to design devices such that they are magnetic-flux biased through passing a current through a flux-bias line instead of applying a global magnetic field. If the noise originates from the magnet itself, this could potentially enhance the stability of the signal.

More broadly speaking, given further research, the requirements for inducing MZMs in superconducting circuits, like the ones of the devices discussed here, could likely be made more clear. In the future, if MZMs could be activated reliably and parameters such as E_M could be measured, topological quantum computation would be one step closer to realization.

Bibliography

- [1] M. A. Nielsen and I. L. Chuang. *Quantum Computation and Quantum Information: 10th Anniversary Edition*. Cambridge University Press, 2010.
- [2] D. P. DiVincenzo. The physical implementation of quantum computation. *Fortschr. Phys.*, 48:2000, 2000.
- [3] J. Clarke and F. K. Wilhelm. Superconducting quantum bits. *Nature*, 453(7198):1031–1042, 2008.
- [4] J. Koch, T. M. Yu, J. Gambetta, A. A. Houck, D. I. Schuster, J. Majer, A. Blais, M. H. Devoret, S. M. Girvin, and R. J. Schoelkopf. Charge-insensitive qubit design derived from the Cooper pair box. *Physical Review A*, 76(4), 2007.
- [5] A. Blais, R.-S. Huang, A. Wallraff, S. M. Girvin, and R. J. Schoelkopf. Cavity quantum electrodynamics for superconducting electrical circuits: An architecture for quantum computation. *Physical Review A*, 69(6), 2004.
- [6] M. Leijnse and K. Flensberg. Introduction to topological superconductivity and Majorana fermions. *Semiconductor Science and Technology*, 27(12):124003, 2012.
- [7] V. Mourik, K. Zuo, S. M. Frolov, S. R. Plissard, E. P. A. M. Bakkers, and L. P. Kouwenhoven. Signatures of Majorana Fermions in Hybrid Superconductor-Semiconductor Nanowire Devices. *Science*, 336(6084):1003–1007, 2012.
- [8] E. Ginossar and E. Grosfeld. Microwave transitions as a signature of coherent parity mixing effects in the Majorana-transmon qubit. *Nature Communications*, 5:4772, 2014.
- [9] A. Blais. Quantum computing with superconducting qubits. Lecture at Canadian Summer School on Quantum Information 2012, University of Waterloo. Retrieved in 2018 from https://youtu.be/t5nxusm_Umk and https://youtu.be/KOZCPl_DyDU, 2012.
- [10] V. Bouchiat, D. Vion, P. Joyez, D. Esteve, and M. H. Devoret. Quantum coherence with a single Cooper pair. *Physica Scripta*, 1998(T76):165, 1998.

- [11] Y. Nakamura, Y. A. Pashkin, and J. S. Tsai. Coherent control of macroscopic quantum states in a single-Cooper-pair box. *Nature*, 398(6730):786–788, 1999.
- [12] J. A. Schreier, A. A. Houck, J. Koch, D. I. Schuster, B. R. Johnson, J. M. Chow, J. M. Gambetta, J. Majer, L. Frunzio, M. H. Devoret, S. M. Girvin, and R. J. Schoelkopf. Suppressing charge noise decoherence in superconducting charge qubits. *Physical Review B*, 77(18):180502, 2008.
- [13] T. W. Larsen, K. D. Petersson, F. Kuemmeth, T. S. Jespersen, P. Krogstrup, J. Nygård, and C. M. Marcus. Semiconductor-Nanowire-Based Superconducting Qubit. *Physical Review Letters*, 115(12), 2015.
- [14] L. Casparis, T. W. Larsen, M. S. Olsen, F. Kuemmeth, P. Krogstrup, J. Nygård, K. D. Petersson, and C. M. Marcus. Gatemon Benchmarking and Two-Qubit Operations. *Physical Review Letters*, 116(15), 2016.
- [15] A. Kringsøj, L. Casparis, M. Hell, T. W. Larsen, F. Kuemmeth, M. Leijnse, K. Flensberg, P. Krogstrup, J. Nygård, K. D. Petersson, and C. M. Marcus. Anharmonicity of a superconducting qubit with a few-mode Josephson junction. *Physical Review B*, 97(6):060508, 2018.
- [16] A. Y. Kitaev. Unpaired Majorana fermions in quantum wires. *Physics-Uspekhi*, 44(10S):131, 2001.
- [17] R. M. Lutchyn, J. D. Sau, and S. Das Sarma. Majorana Fermions and a Topological Phase Transition in Semiconductor-Superconductor Heterostructures. *Physical Review Letters*, 105(7):077001, 2010.
- [18] Y. Oreg, G. Refael, and F. von Oppen. Helical Liquids and Majorana Bound States in Quantum Wires. *Physical Review Letters*, 105(17):177002, 2010.
- [19] M. T. Deng, C. L. Yu, G. Y. Huang, M. Larsson, P. Caroff, and H. Q. Xu. Anomalous Zero-Bias Conductance Peak in a Nb–InSb Nanowire–Nb Hybrid Device. *Nano Letters*, 12(12):6414–6419, 2012.

- [20] A. Y. Kitaev. Fault-tolerant quantum computation by anyons. *Annals of Physics*, 303(1):2–30, 2003.
- [21] K. Yavilberg, E. Ginossar, and E. Grosfeld. Fermion parity measurement and control in Majorana circuit quantum electrodynamics. *Physical Review B*, 92(7), 2015.
- [22] B. van Heck. Personal communication, 2018.
- [23] J. G. Kroll, F. Borsoi, K. L. van der Enden, W. Uilhoorn, D. de Jong, M. Quintero-Pérez, D. J. van Woerkom, A. Bruno, S. R. Plissard, D. Car, E. P. A. M. Bakkers, M. C. Cassidy, and L. P. Kouwenhoven. Magnetic field resilient superconducting coplanar waveguide resonators for hybrid cQED experiments. *arXiv:1809.03932*, 2018.
- [24] C. J. Foot. *Atomic Physics*. Oxford University Press, 2005.
- [25] S. M. Sze and M.-K. Lee. *Semiconductor Devices: Physics and Technology*. John Wiley & Sons Singapore Pte. Limited, 2012.
- [26] J. Stehlik, Y.-Y. Liu, C. Eichler, T. R. Hartke, X. Mi, M. J. Gullans, J. M. Taylor, and J. R. Petta. Double Quantum Dot Floquet Gain Medium. *Physical Review X*, 6(4), 2016.
- [27] P. Krogstrup, N. L. B. Ziino, W. Chang, S. M. Albrecht, M. H. Madsen, E. Johnson, J. Nygård, C. M. Marcus, and T. S. Jespersen. Epitaxy of semiconductor–superconductor nanowires. *Nature Materials*, 14(4):400–406, 2015.
- [28] F. Pobell. *Matter and Methods at Low Temperatures*. Springer, Berlin; New York, 3rd edition, 2007.